Acta Oceanol. Sin., 2020, Vol. 39, No. 3, P. 81–89
https://doi.org/10.1007/s13131-019-1531-2
http://www.hyxb.org.cn
E-mail: hyxbe@263.net

Surface warming patterns dominate the uncertainty in global water vapor plus lapse rate feedback

Jingchun Zhang[1], Jian Ma[2]*, Jing Che[1], Zhenqiang Zhou[3], Guoping Gao[4]

[1] College of Marine Sciences, Shanghai Ocean University, Shanghai 201306, China

[2] School of Oceanography, Shanghai Jiao Tong University, Shanghai 200030, China

[3] Institute of Atmospheric Sciences, Fudan University, Shanghai 200438, China

[4] College of Marine Science and Engineering, Shanghai Maritime University, Shanghai 201306, China

Received 28 April 2019; accepted 3 June 2019

Abstract

Climate feedbacks have been usually estimated using changes in radiative effects associated with increased global-mean surface temperature. Feedback uncertainties, however, are not only functions of global-mean surface temperature increase. In projections by global climate models, it has been demonstrated that the geographical variation of sea surface temperature change brings significant uncertainties into atmospheric circulation and precipitation responses at regional scales. Here we show that the spatial pattern of surface warming is a major contributor to uncertainty in the combined water vapour-lapse rate feedback. This is demonstrated by computing the global-mean radiative effects of changes in air temperature and relative humidity simulated by 31 climate models using a methodology based on radiative kernels. Our results highlight the important contribution of regional climate change to the uncertainty in climate feedbacks, and identify the regions of the world where constraining surface warming patterns would be most effective for higher skill of climate projections.

Key words: surface warming patterns, uncertainty, water vapor feedback, lapse rate feedback, relative humidity, air temperature, radiative kernels

Citation: Zhang Jingchun, Ma Jian, Che Jing, Zhou Zhenqiang, Gao Guoping. 2020. Surface warming patterns dominate the uncertainty in global water vapor plus lapse rate feedback. Acta Oceanologica Sinica, 39(3): 81–89, doi: 10.1007/s13131-019-1531-2

1 Introduction

Significant changes in climate are expected in response to anthropogenic global warming. Determining the magnitude of these changes is complicated by the presence of climate feedbacks that can amplify (positive feedback) or diminish (negative feedback) warming effects. For example, higher air temperature due to increased greenhouse gases by human activity is associated with more atmospheric water vapour. Since this is also a greenhouse gas, its increase provides a positive radiative feedback (Cess, 2005), which can about triple the sensitivity of surface temperature to greenhouse gas forcing according to projections with climate models (Held and Soden, 2000). Moreover, in the projections, tropical tropospheric warming increases with height from the surface as the lapse rates decrease (Ma et al., 2012). This further strengthens the water vapour feedback, but the enhanced longwave emission at higher temperatures in the upper troposphere introduces a negative lapse rate feedback (Bony et al., 2006).

Since temperature and water vapor changes are tightly coupled in models, water vapor and lapse rate feedbacks may both be interpreted as consquences of tropospheric warming, i.e., the higher tropospheric warming (more negative lapse rate feedback), the larger tropospheric moistening (more positive water vapor feedback). Thus, these two feedbacks are negatively correlated among models, aka partially offset each other, and have been often combined in previous studies (Bony et al., 2006; Soden and Held, 2006; Soden et al., 2008). This combined feedback, however, is subject to significant spread among the models, which reduces the reliability of climate projections in a way that is poorly understood (Held and Shell, 2012).

The present paper focuses on quantitatively attributing the uncertainty of the water vapour plus lapse rate feedback. Here, uncertainty of a feedback is defined as the ratio between the inter model spread in estimates and the corresponding ensemble average. Atmospheric changes in specific humidity (q) involve changes in air temperature (T) and relative humidity (RH) (Colman, 2004; Held and Soden, 2006). If $[X]$ denotes the global-mean radiative effect at the top of atmosphere due to changes in X, then the following symbolic relationship holds for the combined effect of water vapour and lapse rate (LR) changes,

$$[q] + [LR] = [RH] + \{[T] + [LR]\}\,, \tag{1}$$

where LR can be defined as the departure of T from surface temperature (T_s). We can estimate the right-hand-side of Eq. (1) using total-sky radiative kernels(Soden and Held 2006; Soden et al.,

Foundation item: The National Natural Science Foundation of China under contract No. 41675070; the Shanghai Eastern Scholar Program under contract No. TP2015049; the Expert Development Fund under contract No. 2017033; the China Scholarship Council under contract No. 201506330007.

*Corresponding author, E-mail: Jian.Ma@SJTU.edu.cn

2008; Held and Shell, 2012). In here we apply those based on the Geophysical Fluid Dynamics Laboratory (GFDL) AM2p12b model (The GFDL Global Atmospheric Model Development Team, 2004). These kernels provide the spatial weights for the global averaging of changes in X [Eq. (5) in Section 2.2 is the precise expression of Eq. (1)].

The radiative effect of changes in T, which plays a major role in the water vapour feedback (Soden et al., 2008), can be estimated with the water vapour kernel (Fig. 1a). The combined term $\{[T]+[LR]\}$ can be obtained with the water vapour and air temperature kernels (Fig. 1b). The terms in the bracket, however, tend to have the same order of magnitude and opposite signs (Soden et al., 2008). This leads to partial cancellation (Fig. 1c) (Soden and Held, 2006), which results in a significantly enhanced role of RH in Eq. (1) (Held and Shell, 2012). We will show that $[RH]$ results primarily from changes at regional scales, of which the global-mean is computed by using the weights provided by the water vapour kernel taking longwave and shortwave radiation into account. This regional *RH* response is further traced to spatial patterns of sea surface temperature (SST) change, which govern regional convective adjustments (Xie et al., 2010; Ma and Xie, 2013) and produce significant uncertainty in rainfall projections.

In the following we evaluate the terms in Eq. (1) using the output from Representative Concentration Pathway 4.5 (RCP 4.5) simulations by 31 models participating in the Coupled Model Intercomparison Project phase 5 (CMIP5) (Taylor et al., 2012). Required by feedback assessment (Soden and Held, 2006; Soden et al., 2008; Held and Shell, 2012), all changes (defined as the difference between the simulated 10-year averages for 2006–2015 and 2089–98) are normalized by the global-mean surface warming. One important feature of our approach is the emphasis on the inter-model differences among the radiative effects due to the geographical distributions of simulated changes.

2 Data and methods

2.1 *Data*

RCP 4.5 simulations produced by 31 CMIP5 models (Taylor et al., 2012) are used in this study. The models provide various lengths of simulations with the future radiative forcing stabilized at 4.5 W/m^2 in 2100. We analyze one realization ("r1i1p1") from each model during the period 2006–2098, and changes are calculated as the difference between the 10-year averages for 2006–2015 and 2089–2098. The models include ACCESS1.0, ACCESS1.3, BCC-CSM1.1, BCC-CSM1.1-M, BNU-ESM, CanESM2, CCSM4, CESM1-BGC, CESM1-CAM5, CMCC-CM, CMCC-CMS, CNRM-CM5, CSIRO-Mk3.6.0, FIO-ESM, GFDL-CM3, GFDL-ESM2G, HadGEM2-AO, HadGEM2-CC, HadGEM2-ES, INM-CM4, IPSL-CM5A-LR, IPSL-CM5A-MR, IPSL-CM5B-LR, MIROC5, MIROC-ESM, MIROC-ESM-CHEM, MPI-ESM-LR, MPI-ESM-MR, MRI-CGCM3, NorESM1-M, NorESM1-ME. Because climate feedbacks are expressed as responses of the top-of-atmosphere radiative flux to changes driven by 1°C global-mean sur-

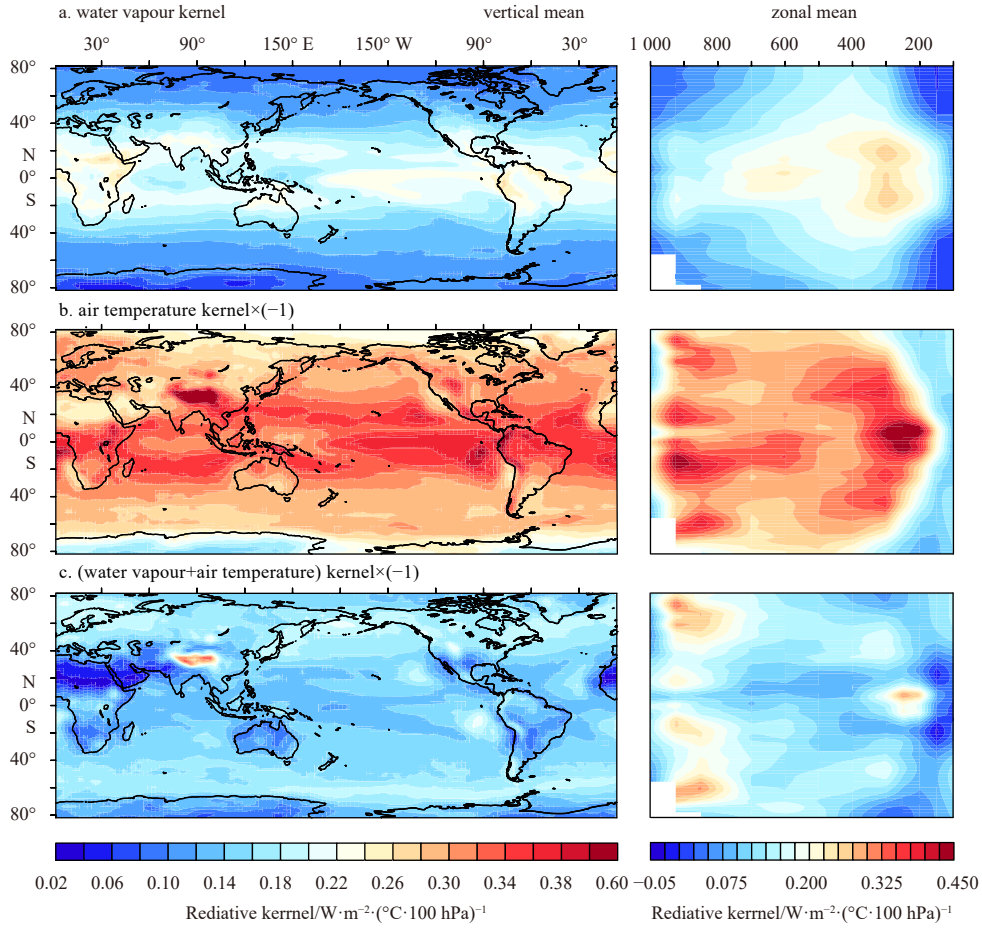

Fig. 1. Annual mean vertically (100–1 000 hPa, left) and zonally (right) averaged total-sky radiative kernels [W/(m^2·°C·100 hPa)]. They are computed with the GFDL AM2p12b model.

face warming, all changes are normalized by the global-mean surface warming before the computations of ensemble means, spreads, kernels, SVD, and regressions.

2.2 *Methods*

2.2.1 *Decomposition of water vapour change*

If q is specific humidity meaning the mass of water vapour per unit mass, and q_s is saturation specific humidity, then RH is defined as the percentage of water vapour compared to the one at saturation, i.e., $q = RH \cdot q_s$. If δ denotes change,

$$\ln q = \ln RH + \ln q_s \Rightarrow \frac{\delta q}{q} = \frac{\delta RH}{RH} + \frac{\delta q_s}{q_s}. \tag{2}$$

The Clausius-Clapeyron relation (Held and Soden, 2006), $\frac{\delta q_s}{q_s} = \frac{\delta e_s}{e_s} = \alpha \delta T$, can be inserted into Eq. (2) to obtain:

$$\frac{\delta q}{q} = \frac{\delta RH}{RH} + \alpha \delta T. \tag{3}$$

where $\alpha = \frac{L}{R_v T^2}$, where $L = \begin{cases} 2.50 \times 10^6 \text{ J/kg}, & \text{for liquid} \\ 2.83 \times 10^6 \text{ J/kg}, & \text{for ice} \end{cases}$ represents the latent heat of water, and $R_v = 461.5 \text{ J/(K} \cdot \text{kg)}$ is the gas constant of water vapour.

2.2.2 *The radiative kernels*

Radiative kernels (Soden and Held, 2006; Soden et al., 2008; Held and Shell, 2012) provide a simple and accurate methodology to convert the responses of specific climate factors to their corresponding radiative effects and to quantify climate feedbacks across various models in a consistent way. The kernels use incremental changes in the feedback variables to describe the differential responses of the top-of-atmosphere radiative flux. Such conversions act as spatial weights for changes in climate variables before global averaging. Here we use the total-sky radiative kernels based on the GFDL AM2p12b model (The GFDL Global Atmospheric Model Development Team, 2004), and the water vapour kernel includes both longwave and shortwave radiation.

To calculate a specific feedback, one needs to: (1) normalize the change of the climate variable with global-mean surface warming; (2) convert the normalized value into unit of temperature; (3) multiply it by the radiative kernel; (4) perform vertical integration and horizontal averaging across the globe. We note the entire procedure as $K_x[X]$ in the following. For example, the water vapour feedback can be examined with the above-mentioned decomposition,

$$K_w = \left[\frac{\delta q}{\alpha q} = \frac{\delta RH}{\alpha RH} + \delta T\right] \Rightarrow K_w \left[\frac{\delta q}{\alpha q}\right] = K_w \left[\frac{\delta RH}{\alpha RH}\right] + K_w[\delta T]. \tag{4}$$

As shown in Fig. 1a, the generally positive water vapour kernel has highest sensitivity for tropical convective regions in the upper troposphere, since clouds mask the low-level moistening.

2.2.3 *Offset of water vapour feedback by lapse rate feedback*

The lapse rate is defined as $(T - T_s)$, so its feedback has the form, $K_T[\delta T - \delta T_s] = K_T[\delta T] - K_T[\delta T_s]$. The air temperature kernel is negative (Fig. 1b), with maxima at the space-exposing cloud tops of tropical deep convection-detrained cirrus and on the cloud-topped boundary layer. The kernel-weighted global mean of surface warming has a rather weak influence on the inter-model variation, only canceling 8% of the direct T effect.

Combined with the above water vapour feedback, one can obtain the expression of the water vapour plus lapse rate feedback.

$$K_w \left[\frac{\delta q}{\alpha q}\right] + K_T[\delta T - \delta T_s] = K_w \left[\frac{\delta RH}{\alpha RH}\right] + (K_w + K_T)[\delta T] - K_T[\delta T_s], \tag{5}$$

which is the precise form of Eq. (1). Since K_w is positive but K_T is negative, and the latter is stronger than the former, their sum is weakly negative (Fig. 1c). Indeed, the inter-model spread of the lapse rate feedback [0.27 W/(m^2·°C)] is 1.5 times that of the T effect in water vapour feedback [0.18 W/(m^2·°C)], with a very strong negative correlation (–0.996). This results in significant offset when combined [0.09 W/(m^2·°C)], amplifying the relative importance of the RH effect. Yet the ensemble mean of the combined feedback is still positive because of the aforementioned reduction of the lapse rate feedback by surface warming.

2.2.4 *Inter-model statistical analysis*

These analyses are based on dynamic interpretations in literature (Xie et al., 2010; Ma and Xie, 2013; Kosaka and Xie, 2013; Ding et al., 2014; Perlwitz et al., 2015; Wang et al., 2017) to locate the origin of uncertainty, specifically by replacing conventional time series with the model series. Inter-model correlation and regression are performed for T change (3-D) on tropical-mean surface warming. For the attribution of uncertainties in climate feedbacks, the variances explained by different factors are estimated as squares of the inter-model correlations with the total effect.

SVD returns the covariant modes of two variables. We performed an inter-model SVD for percentage change of RH (3-D) on SST pattern change (2-D) in the tropics (40°S–40°N). We then used the three-dimensional patterns of the RH modes to calculate partial feedback parameters and made linear combination of these parameters with the corresponding principle components to reconstruct the RH effect for each model as

$$K_w \left[\frac{\delta RH}{\alpha RH}\right] : \sum_{i=1}^{m} \lambda_i K_w \left[\frac{S_i}{\alpha}\right], \tag{6}$$

where λ_i and S_i are the principle component and spatial modes of $\frac{\delta RH}{RH}$, and m denotes the total number of the leading modes. After reordering the modes according to the variances they explain individually, the cumulative variance of the reconstruction was calculated based upon the correlations between the cumulative combinations of leading modes and the RH effect.

3 Effects of different factors on uncertainty in the water vapor plus lapse rate feedback

We start with the global-mean values. The annual- and ensemble-mean water vapour plus lapse rate feedback is 1.1 W/(m^2·°C), with contribution from the T changes amounting to 1.2 W/(m^2·°C). The global-mean changes in RH have very small magnitudes (0.02%±0.28%), and the ensemble-mean of their radiative effect is weak [–0.1 W/(m^2·°C)]. However, the inter-model spreads in the effects of RH and T changes are comparable [0.03 W/(m^2·°C) and 0.09 W/(m^2·°C), respectively], so the uncertainty in the former

(30%) is 4 times that in the latter (7.5%). If calculated directly as squares of the inter-model correlations, the variances explained by the effects of *RH* and *T* changes are 61% and 81%, respectively, while their covariance is 21% so their actual contributions are 40% and 60%, respectively (Fig. 2a). In total, the combined effect of *RH* and *T* changes accounts for 99% of the uncertainty in the water vapour plus lapse rate feedback. In the following we concentrate on annual-mean values because monthly-mean data provide similar results (Fig. 3a).

3.1 *Air temperature*

Figures 1 and 4 show that the water vapor and lapse rate feedbacks both are important over the tropics where water cycle is strongest, which not only holds maximum water vapor but also generate deep convective clouds emitting strong longwave radiation. In magnitude, the lapse rate feedback dominates over the water vapor feedback. However, low clouds in the extratropics make big difference between the two feedbacks, because they prohibit the moistening of upper troposphere but enhance the longwave emission. These regional features are important for the *T* effect, which uses the difference between absolute values of the two kernels as its spatial weight.

Figure 2b shows that the uncertainty in the feedback induced by *T* changes can be expressed (74%) as a function of the change in T_s averaged in an extended tropical domain (40°S–40°N). In the tropics, *T* changes have weak spatial variations (Ma et al., 2012) and are closely coupled to area-average increase of T_s because fast atmospheric wave actions smooth out the footprints of

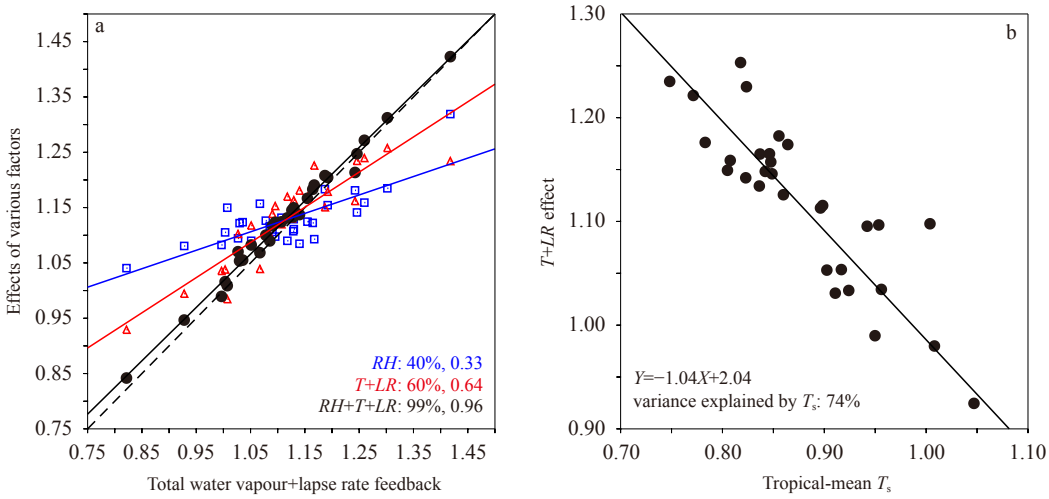

Fig. 2. a. Inter-model scatterplot of the decomposition of the water vapour plus lapse rate feedback (W/(m²·°C)). The variances explained by various factors are calculated from squares of the inter-model correlations and marked with slopes of the regressions in colours corresponding to the factors. b. Scatterplot between the temperature plus lapse rate effect and tropical-mean (40°S–40°N) T_s change (°C). Here we use the annual-mean results of the radiative kernels, and 31 CMIP5 simulations along RCP4.5 normalized by the global-mean surface warming.

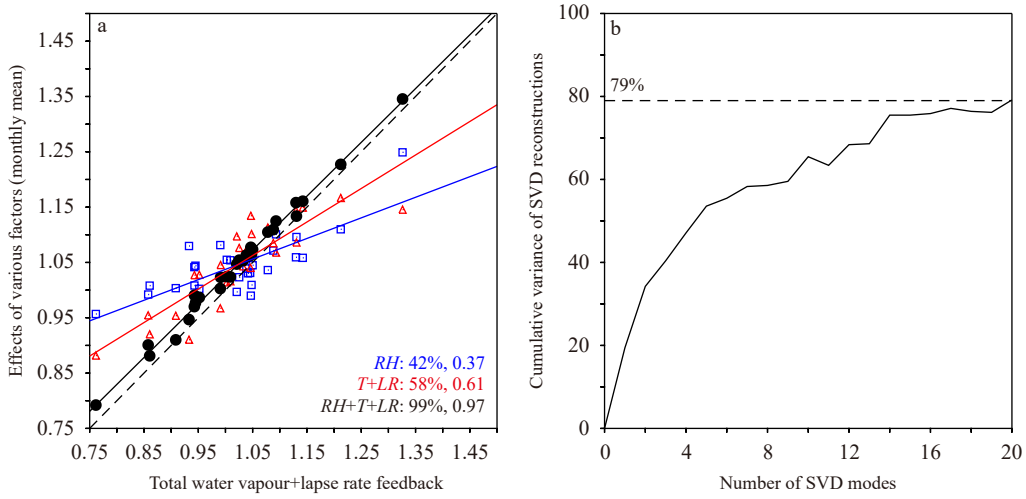

Fig. 3. a. Inter-model scatterplot of the decomposition of water vapor plus lapse rate feedback (W/(m²·°C)). Same as in Fig. 2a, but based on the monthly-mean radiative kernels and CMIP5 output. The variances explained by various factors are calculated from squares of the inter-model correlations and marked with slopes of the regressions. b. The cumulative variance of the inter-model SVD reconstruction in Fig. 7a. The squares of correlations between the RH effect and cumulative combinations of the leading modes are calculated after the modes are reordered with the variances they explain individually.

uneven surface warming (Xie et al., 2010). In the extratropics poleward of 40° latitude, coupling with the surface is weak (Soden and Held, 2006) due to the dominance of synoptic eddies. However, the three-dimensional (3-D) structure of changes in atmospheric temperature needs to be examined for a better understanding of this vertical decoupling.

Let us consider in more spatial detail the inter-model associations between changes in T and tropically averaged T_s. Figure 4c is a latitude-longitude plot of the vertical mean of corresponding regressions. Normalization by the global-mean surface warming makes the globally averaged value of T_s changes equal 1 in all models, so that a seesaw pattern between tropics and extratropics is evident in the inter-model variations of these changes. Regions where the tropical influence is weaker extend eastward from Greenland to the northern Eurasian continent, particularly over the North Atlantic-Arctic adjacent seas. These geographical differences are associated with large inter-model standard deviation of T_s change (grids in Fig. 4c), which are affected by biases in the simulation of ocean heat transport (Jackson et al., 2016; Mahlstein and Knutti, 2011) and polar amplification of the global warming (Feldl and Roe, 2013). This argument is supported by the high global spatial correlation of –0.71 shown in Fig. 4c.

While a seasaw pattern is reasonable, it does not garantee the control of global temperature by trpical T_s. Indeed, the figure captures atmospheric teleconnections between tropics and high latitudes, including the Pacific-North American pattern with pronounced positive response in northwestern North America (Kosaka and Xie, 2013; Ding et al., 2014; Perlwitz et al., 2015; Wang et al., 2017). Changes in the storm tracks over the Southern Ocean are also visible. In addition, Figures 4a and b reveal that the pathway of the teleconnection is through upper troposphere with latitude-height plots of the zonal mean of the correlations/regressions of changes in T on tropically averaged T_s. A poleward export of latent energy from the tropics (Feldl and Roe, 2013), possibly by stationary/transient eddies (Kosaka and Xie, 2013), is apparent in the extra-tropical upper troposphere, especially in the Southern Hemisphere.

Such a tropics-originated energy export reduces the local coupling between surface and atmosphere in the extratropics, and helps to anchor the global-mean T change to the tropically averaged T_s with the inter-model variance explained by 81%. This value is slightly higher than that for the aforementioned kernel-weighted mean because higher weights (Fig. 1c) are applied by the temperature kernel to the top of low clouds. Thus, regional climate change, which determines the difference in surface warming between the tropics and extratropics, is a major source of uncertainty in the T-induced water vapour plus lapse rate feedback.

3.2 *Relative humidity*

Turning now to RH, the vertically averaged values of its percentage change show variations of up to 5% (Fig. 5a) and large-

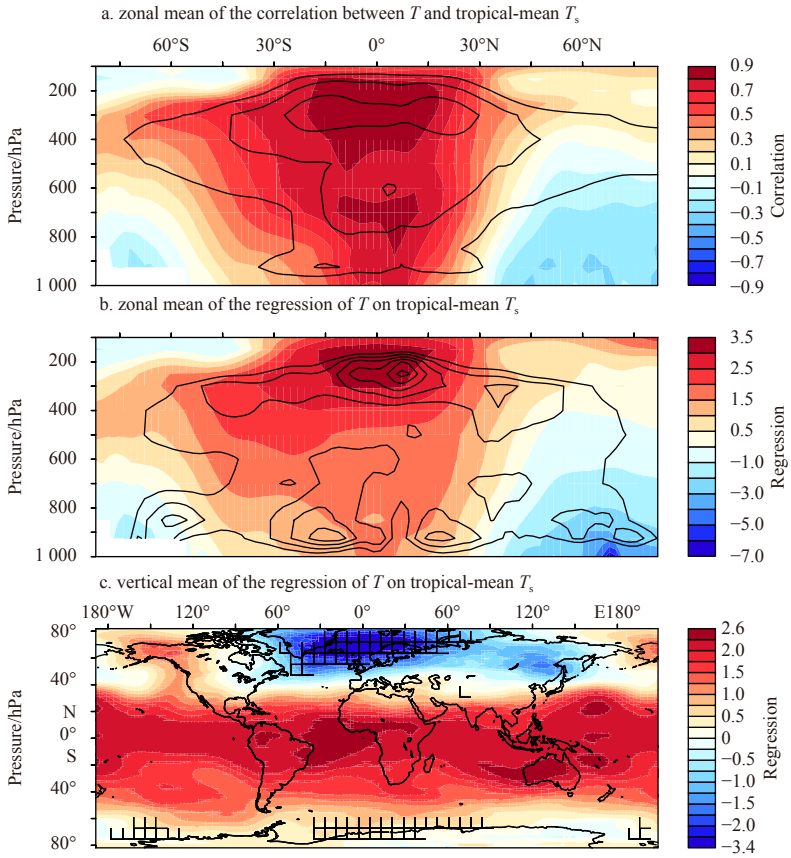

Fig. 4. Inter-model associations between annual-mean atmospheric temperature change (3-D) and tropical-mean (40°S–40°N) surface warming among the 31 CMIP 5 simulations along RCP 4.5, normalized by the global-mean surface warming. The zonal (a, b) and vertical (c) averages are performed after calculating the correlations (a)/regressions (b, c). Water vapour and temperature kernels (black) are overlaid in a and b, respectively. Areas with large inter-model standard deviations of surface warming (>1.5°C) are marked with grids in c.

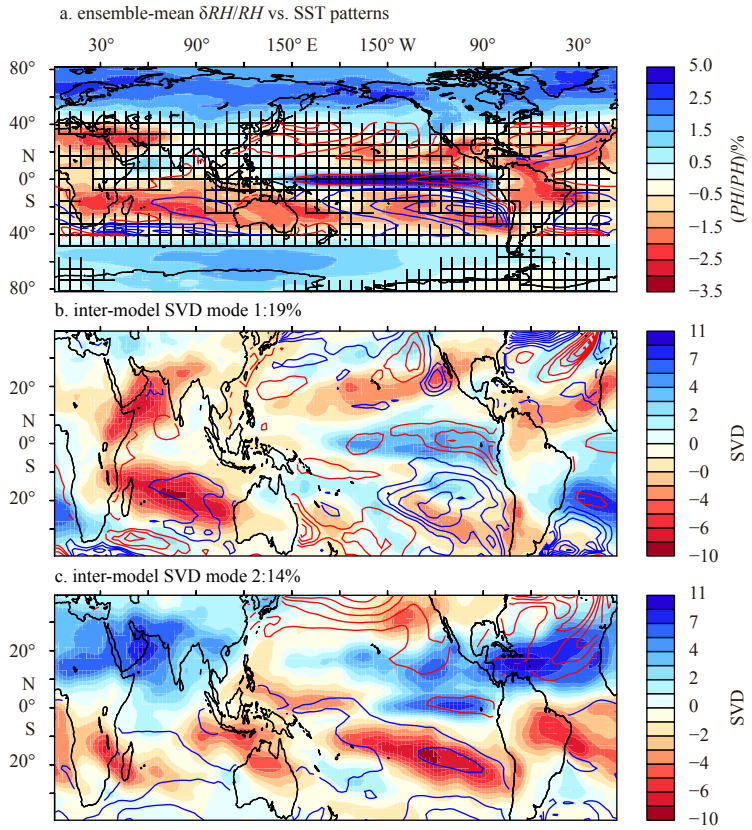

Fig. 5. Vertically (100–1 000 hPa) averaged percentage *RH* change (shading, %) and SST warming patterns (contours, °C; contour interval: 0.1°C; red positive, blue negative; 0 omitted) in ensemble mean (a) and leading modes of the inter-model SVD (b, c) between them (3-D). The SVD is performed in the tropics (40°S–40°N) and SST pattern change is defined as deviations from the tropical-mean SST increase. Gridded areas in a mark where inter-model spread of RH exceeds 3 times the ensemble mean. Here we use the annual-mean results of the 31 CMIP 5 simulations along RCP 4.5, normalized by the global-mean surface warming.

scale spatial patterns (Wright et al., 2010; Sherwood et al., 2010a). The global spatial correlation between these percentage changes and those of local water vapour change ($\delta q/q$) in Eq. (3) (see Section 2.2) is 0.61 (0.58 for zonal mean). Recent observational data suggest that changes of such magnitude can exert considerable effects on the water vapour feedback (Solomon et al., 2010) while directly affecting many important aspects of climate such as cloud formation and precipitation efficiency (Sherwood et al., 2010b). There is a significant RH reduction in the tropical upper troposphere (Fig. 6a) due to tropopause rise (Sherwood et al., 2010b), and possibly a weakening of the tropical circulation (Ma et al., 2012). The drying is weaker in the subtropics in association with a tropical expansion during global warming(Sherwood et al., 2010b). Since the water vapour kernel applies strongest weights in the tropical upper troposphere, the overall RH effect is negative [–0.1 W/(m^2·°C) in the ensemble mean] so that analyses assuming a fixed RH would likely overestimate the water vapour feedback (Minschwaner and Dessler, 2004).

The changes in *RH* have larger magnitudes in the tropics (Fig. 5a and Fig. 6a). The pattern of these changes over the oceans has a "warmer-get-wetter" signature (Xie et al., 2010) (Fig. 5a). This means a dynamic redistribution of convection in association with deviations in the SST changes from their tropical-mean (40°S–40°N) values. In particular, the SST warming peak in the equatorial Pacific is collocated with enhanced *RH*, with the maximum at 500 hPa (Figs 6a, b). The relative cooling center in the southeastern subtropical Pacific is collocated with reduced *RH*. The south-to-north gradient in the SST warming generates an inter-hemispheric asymmetry in the tropical upper-tropospheric and subtropical *RH* reduction (Figs 6a, b). In the tropics, the horizontal correlation between *RH* and the SST patterns is 0.45, and the zonal-mean correlation is 0.69.

The inter-model spread in *RH* changes can be higher than three times the ensemble mean in vast tropical regions (Fig. 5a and Fig. 6a). The regional SST warming is also quite diverse among the models (Ma and Xie, 2013). It is therefore useful to assess the extent to which the pattern of *RH* changes covaries with that of SST changes. For this, we perform an inter-model singular value decomposition (SVD) between the values of SST and percentage *RH* change in the region 40°S–40°N. The first leading mode features a meridionally symmetric pattern in general, and its weighted global means by the water vapour kernel explain 19% of the variance in the RH-induced feedback. The enhanced equatorial SST warming (Fig. 5b) leads to an *RH* increase peaking at 500 hPa (Figs 6c, d), and a subtropical cooling is collocated with drying. The second mode contributes 14% variance, with an inter-hemispheric asymmetry that warms the surface ocean in the northern subtropics resulting in local increases of moisture (Fig. 5c) throughout the tropospheric column (Figs 6e, f).

The SST warming pattern-involved ocean-atmosphere interactions have been highlight important in water cycle changes under greenhouse warming (Long et al., 2016), as suggested by theoretical diagnostics and numerical experiments (Xie et al., 2010). The above two leading modes represent the major meridional

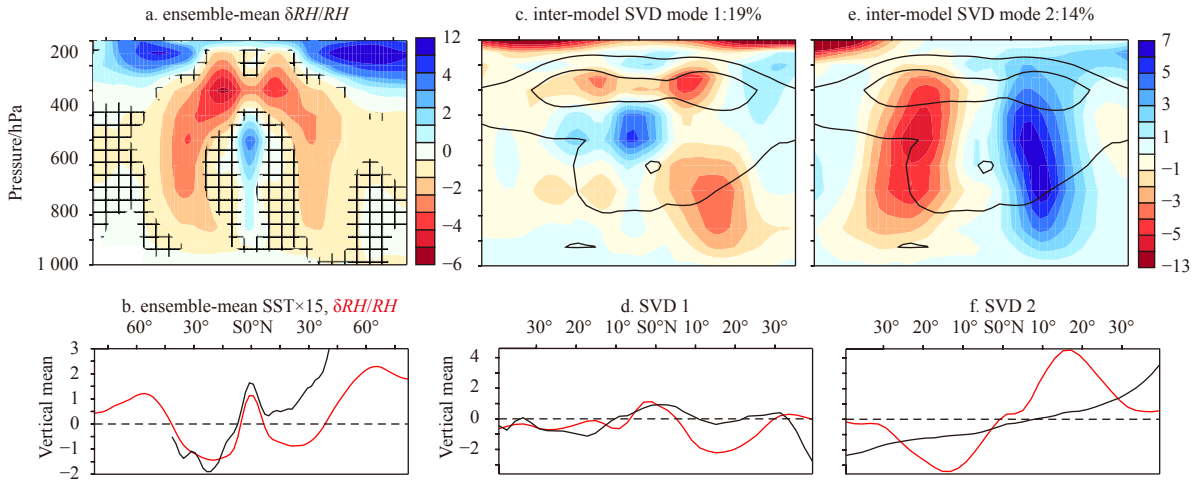

Fig. 6. Zonally averaged ensemble mean (a, b) and leading modes of the inter-model SVD (3-D)(c–f) between the percentage *RH* change (%) and SST warming patterns (°C). The SVD is performed in the tropics (40°S–40°N) and SST pattern change is defined as deviations from the tropical-mean SST increase. *RH* mean and modes (shadings) are presented in the upper panel, with gridded areas in a marking where inter-model spread exceeds 3 times of the ensemble mean, and water vapor kernel (black) overlaid in c and e. Vertical (100–1 000 hPa) means of *RH* (red) and zonal means of SST patterns (black) are shown in the lower panel. Here we use the annual-mean results of the 31 CMIP 5 simulations along RCP 4.5, normalized by the global-mean surface warming.

symmetric and asymmetric characteristics of SST pattern change. The first mode implies an enhanced Hadley circulation on either side of the equator, driven by the equatorial peak of SST warming. The second features positive (negative) anomalous SST in the Northern (Southern) Hemisphere, which causes a cross-equatorial circulation that represents an enhanced (weakened) Hadley cell south (north) of the equator. The inter-model variance in the effect of RH changes associated with these two SST modes is 34%, which is consistent with that for regional precipitation change (Ma and Xie, 2013).

The cumulative variance explained by increasing the number of leading modes reaches a plateau with about 14 modes (Fig. 3b), while the total variance explained by the first 20 modes is 79% (Fig. 7a). It is noteworthy that the first several modes matter most, and combining 20 modes changes little from 14 modes. The reconstructed RH effect has a slightly stronger spread (inter-model slope of 1.29) because it excludes the moderate values in the extratropics (Fig. 5a and Fig. 6a). Our analysis with the SVD suggests that regional climate change, again, dominates the uncertainty in the RH-induced water vapour plus lapse rate feedback.

The aforementioned 21% covariance between the effects of RH and *T* changes deserves future investigation. For example, Figure 5a shows that RH over tropical land decreases substantially due to amplified air warming, because less water is present for evaporative cooling than over the tropical oceans (Sherwood et al., 2010a, 2010b). This arises because on long time-scales, almost all moisture over land is advected from the oceans, which is

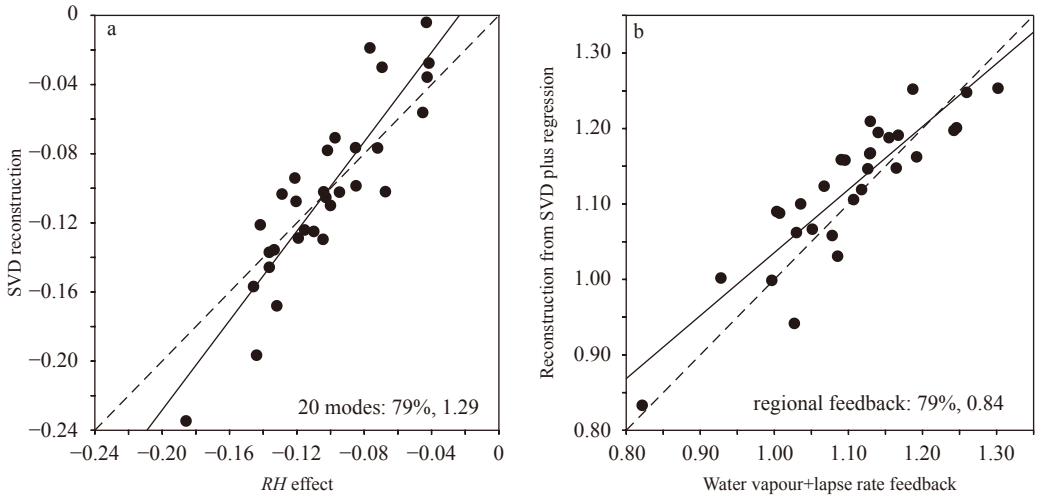

Fig. 7. *RH* effect (W/(m²·°C))reconstructed by the first 20 SVD modes (a), and water vapour plus lapse rate feedback (W/(m²·°C)) reconstructed by combining the inter-model SVD and regression (b). The SVD is performed between percentage *RH* change and SST patterns, and the regression is for the *T* effect against tropical-mean surface warming. Also marked are the variances (squares of the inter-model correlations) that the reconstructions explain and slopes of the inter-model regressions. Here we use the annual-mean results of the radiative kernels, and 31 CMIP 5 simulations along RCP 4.5 normalized by the global-mean surface warming.

relatively less warmed and unable to support the increased moisture-holding capacity of air over land. Such influence of *T* change may be an important contributor to the 21% uncertainty in the RH effect that remains unexplained by the SST patterns.

4 Summary

We have presented a quantitative attribution of the uncertainty in combined water vapour-lapse rate feedback associated with global warming. Our methodology links the radiative effects in the combined feedback to changes in the geographical patterns of surface temperature. This approach has the distinct advantage over the traditional one, which is based on global-mean surface temperature and is insufficient for understanding uncertainties. According to our results, the RH changes at regional scales and *T* increases in the global mean contribute 40% and 60% to the inter-model variance in the water vapour plus lapse rate feedback, respectively. Although the underlying mechanisms for RH change are not fully known at present (Held and Shell, 2012), our findings suggest that its associated uncertainty is highly coupled to that in the tropical SST patterns through convective adjustments (Xie et al., 2010; Ma and Xie, 2013). The tropical-mean surface warming dominates the *T*-induced feedback, which is negatively tied to the highly uncertain surface warming in the extratropical regions between Greenland and the northern Eurasian continent.

In total, the effects of surface warming patterns on the 3-D atmospheric responses control 79% inter-model variance of the water vapour plus lapse rate feedback (Fig. 7b). This indicates that model dependence of regional climate change (Xie et al., 2015) can play a key role in the uncertainty of global radiative feedback. In particular, cloud changes may be closely coupled to the SST patterns in a way similar to *RH*, resulting in the most complex and uncertain radiative feedback. Such uncertainties could be considerably reduced if spatial variations in surface warming among models were constrained with observations. Some attempts in this direction have been conducted for the tropical oceans (Ma and Yu, 2014; Li et al., 2016; Huang and Ying, 2015), but the North Atlantic-Arctic warming is less well understood at the present time. These findings show the potential to open up a new research horizon and improve the accuracy of projected future global warming.

Acknowledgements

We thank B. J. Soden for developing and providing the data of radiative kernels. We acknowledge various modeling groups for producing and providing output, the PCMDI for collecting and archiving CMIP5 dataset, the WGCM for organizing analysis activity, and the DOE of USA for supporting this dataset with the GO-ESSP. Helpful comments from C. R. Mechoso, G. R. Foltz, S.-P. Xie, W. Cai, and R. Zhang are gratefully appreciated. The Matlab and Ferret programs were used for computations, analyses, and graphics.

References

Bony S, Colman R, Kattsov V M, et al. 2006. How well do we understand and evaluate climate change feedback processes?. Journal of Climate, 19(15): 3445–3482, doi: 10.1175/JCLI3819.1

Cess R D. 2005. Water vapor feedback in climate models. Science, 310(5749): 795–796, doi: 10.1126/science.1119258

Colman R. 2004. On the structure of water vapour feedbacks in climate models. Geophysical Research Letters, 31(21): L21109

Ding Qinghua, Wallace J M, Battisti D S, et al. 2014. Tropical forcing of the recent rapid Arctic warming in northeastern Canada and Greenland. Nature, 509(7499): 209–212, doi: 10.1038/nature13260

Feldl N, Roe G H. 2013. The nonlinear and nonlocal nature of climate feedbacks. Journal of Climate, 26(21): 8289–8304, doi: 10.1175/JCLI-D-12-00631.1

Held I M, Shell K M. 2012. Using relative humidity as a state variable in climate feedback analysis. Journal of Climate, 25(8): 2578–2582, doi: 10.1175/JCLI-D-11-00721.1

Held I M, Soden B J. 2000. Water vapor feedback and global warming. Annual Review of Energy and the Environment, 25: 441–475, doi: 10.1146/annurev.energy.25.1.441

Held I M, Soden B J. 2006. Robust responses of the hydrological cycle to global warming. Journal of Climate, 19(21): 5686–5699, doi: 10.1175/JCLI3990.1

Huang Ping, Ying Jun. 2015. A multimodel ensemble pattern regression method to correct the tropical Pacific SST change patterns under global warming. Journal of Climate, 28(12): 4706–4723, doi: 10.1175/JCLI-D-14-00833.1

Jackson L C, Peterson K A, Roberts C D, et al. 2016. Recent slowing of Atlantic overturning circulation as a recovery from earlier strengthening. Nature Geoscience, 9(7): 518–522, doi: 10.1038/ngeo2715

Kosaka Y, Xie Shangping. 2013. Recent global-warming hiatus tied to equatorial Pacific surface cooling. Nature, 501(7467): 403–407, doi: 10.1038/nature12534

Li Gen, Xie Shangping, Du Yan, et al. 2016. Effects of excessive equatorial cold tongue bias on the projections of tropical Pacific climate change. Part I: the warming pattern in CMIP5 multi-model ensemble. Climate Dynamics, 47(12): 3817–3831

Long Shangmin, Xie Shangping, Liu Wei. 2016. Uncertainty in tropical rainfall projections: Atmospheric circulation effect and the ocean coupling. Journal of Climate, 29(7): 2671–2687, doi: 10.1175/JCLI-D-15-0601.1

Ma Jian, Xie Shangping. 2013. Regional patterns of sea surface temperature change: A source of uncertainty in future projections of precipitation and atmospheric circulation. Journal of Climate, 26(8): 2482–2501, doi: 10.1175/JCLI-D-12-00283.1

Ma Jian, Xie Shangping, Kosaka Y. 2012. Mechanisms for tropical tropospheric circulation change in response to global warming. Journal of Climate, 25(8): 2979–2994, doi: 10.1175/JCLI-D-11-00048.1

Ma Jian, Yu Jinyi. 2014. Linking centennial surface warming patterns in the equatorial Pacific to the relative strengths of the Walker and Hadley circulations. Journal of the Atmospheric Sciences, 71(9): 3454–3464, doi: 10.1175/JAS-D-14-0028.1

Mahlstein I, Knutti R. 2011. Ocean heat transport as a cause for model uncertainty in projected Arctic warming. Journal of Climate, 24(5): 1451–1460, doi: 10.1175/2010JCLI3713.1

Minschwaner K, Dessler A E. 2004. Water vapor feedback in the tropical upper troposphere: Model results and observations. Journal of Climate, 17(6): 1272–1282, doi: 10.1175/1520-0442(2004)017<1272:WVFITT>2.0.CO;2

Perlwitz J, Hoerling M, Dole R. 2015. Arctic tropospheric warming: Causes and linkages to lower latitudes. Journal of Climate, 28(6): 2154–2167, doi: 10.1175/JCLI-D-14-00095.1

Sherwood S C, Roca R, Weckwerth T M, et al. 2010a. Tropospheric water vapor, convection, and climate. Reviews of Geophysics, 48(2): RG2001

Sherwood S C, Ingram W, Tsushima Y, et al. 2010b. Relative humidity changes in a warmer climate. Journal of Geophysical Research: Atmosphere, 115(D9): D09104

Soden B J, Held I M. 2006. An assessment of climate feedbacks in coupled ocean-atmosphere models. Journal of Climate, 19(14): 3354–3360, doi: 10.1175/JCLI3799.1

Soden B J, Held I M, Colman R, et al. 2008. Quantifying climate feedbacks using radiative kernels. Journal of Climate, 21(14): 3504–3520, doi: 10.1175/2007JCLI2110.1

Solomon S, Rosenlof K H, Portmann R W, et al. 2010. Contributions of stratospheric water vapor to decadal changes in the rate of global warming. Science, 327(5970): 1219–1223, doi: 10.1126/science.1182488

Taylor K E, Stouffer R J, Meehl G A. 2012. An overview of CMIP5 and

the experiment design. Bulletin of the American Meteorological Society, 93(4): 485–498, doi: 10.1175/BAMS-D-11-00094.1

The GFDL Global Atmospheric Model Development Team. 2004. The new GFDL global atmosphere and land model AM2-LM2: Evaluation with prescribed SST simulations. Journal of Climate, 17(24): 4641–4673, doi: 10.1175/JCLI-3223.1

Wang Chuanyang, Xie Shangping, Kosaka Y, et al. 2017. Global influence of tropical Pacific variability with implications for global warming slowdown. Journal of Climate, 30(7): 2679–2695, doi: 10.1175/JCLI-D-15-0496.1

Wright J S, Sobel A, Galewsky J. 2010. Diagnosis of zonal mean relative humidity changes in a warmer climate. Journal of Climate, 23(17): 4556–4569, doi: 10.1175/2010JCLI3488.1

Xie Shangping, Deser C, Vecchi G A, et al. 2010. Global warming pattern formation: Sea surface temperature and rainfall. Journal of Climate, 23(4): 966–986, doi: 10.1175/2009JCLI3329.1

Xie Shangping, Deser C, Vecchi G A, et al. 2015. Towards predictive understanding of regional climate change. Nature Climate Change, 5(10): 921–930, doi: 10.1038/nclimate2689